

Supporting Information

Water-steam activation toward oxygen-deficient metal oxides for enhancing zinc ions storage

Experimental Section

1. Synthesis of R- V_2O_5 , V_o - V_2O_5 , and P- V_2O_5

High-purity V_2O_5 has been recovered from vanadium-bearing slag by solvent extraction, of which our group proposed a technique route and have been done pilot-scale and industrial-scale experiment [1-3]. A schematic of the pilot-scale production to recover V_2O_5 from vanadium-bearing slag was shown in Figure S1. The recovery of high-purity V_2O_5 from vanadium-containing solutions by primary amines N1923 was labeled as R- V_2O_5 , and the purity of R- V_2O_5 > 99.9 % (Table S1).

For the preparation of oxygen defective V_2O_5 (labeled as V_o - V_2O_5), the obtained R- V_2O_5 was heated in a tube furnace at the temperature of 460 °C under Ar gas containing water-steam atmosphere. In this work, the according calculated amount of oxygen defects in the V_o - V_2O_5 was ~24.2% based on the fitting areas of peaks in O 1s XPS spectra (Figure S3).

For comparison, the V_2O_5 materials with less defects were prepared under the similar treated process except that without water-steam introduction. The obtained materials were labeled as P- V_2O_5 .

2. Physical characterization

The material phase information was characterized by X-ray diffraction using Bruker (XRD, Cu K α radiation). Raman spectra (Renishaw, inVia, England) were collected using laser light at 532 nm wavelength. The morphology of the samples was examined by field emission scanning electron microscopy (JSM-7800), and transmission electron microscopy (JEOL JEM-2100F). X-ray photoelectron spectroscopy (XPS) measurements were carried out on an X-ray photoelectron spectrometer (Thermo ESCALAB 250Xi) using Al K α . The electron spin resonance (ESR) spectroscopy was carried out by Bruker Magnettech ESR5000 to detect the defect character. ICP-OES (OPTIMA 6300DV (Perkin-Elmer, USA) was employed to analyze the concentration of metal ions with the correlation accuracy of 99.99% for standard curves.

3. Electrochemical measurement

Working electrodes were prepared by mixing active material, acetylene black and polyvinylidene fluoride (PVDF) binder with a weight ratio of 7:2:1 to form a homogenous slurry with N-methyl pyrrolidone (NMP) as the solvent. The obtained slurry was then coated on titanium foil and dried in a vacuum oven at 70 °C. Finally, the active material mass loading per working electrode was about 1-3 mg cm⁻². Glass fiber (Fisher Scientific) and Zn foil (Alfa Aesar, 0.25 mm thick) were employed as separator and

anode, respectively. A 3 M $\text{Zn}(\text{CF}_3\text{SO}_3)_2$ aqueous solution was used as the electrolyte. The CR2016 coin cells were assembled in the air atmosphere to estimate the electrochemical performance. Cyclic voltammetry (CV) tests were carried out on the electrochemical workstation (CHI760D, Shanghai Chenhua). Galvanostatic charge/discharge tests were performed on a LAND-CT2001A in a voltage window from 0.2 to 1.6 V versus Zn^{2+}/Zn at various current densities. The galvanostatic intermittence titration technique (GITT) was also tested on LAND-CT2001A at a current density of 50 mA g^{-1} with a galvanostatic discharge pulse of 10 min and a relaxation of 20 min for each step.



Figure S1. Schematic of the pilot-scale production to recover V_2O_5 from vanadium-bearing slag, with an optical image of recycled high-purity V_2O_5 (labeled as R- V_2O_5).

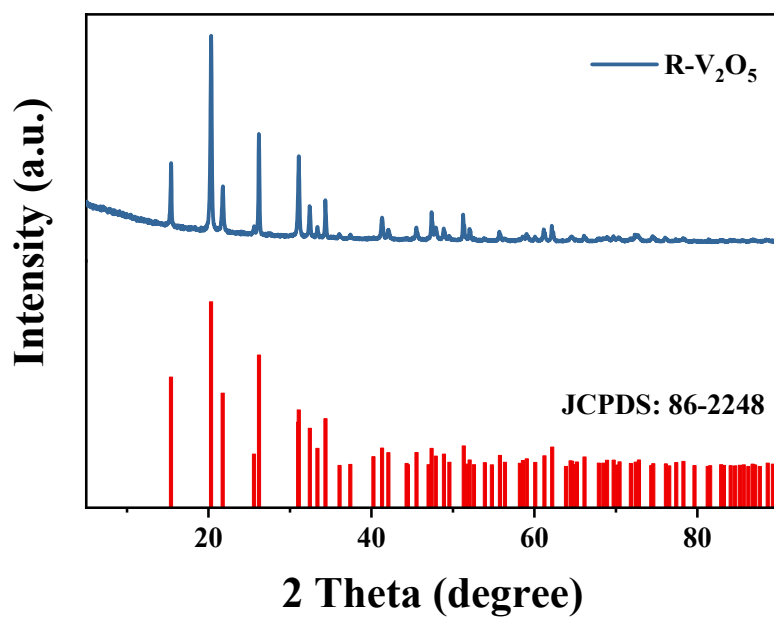


Figure S2. The XRD pattern of the R- V_2O_5 .

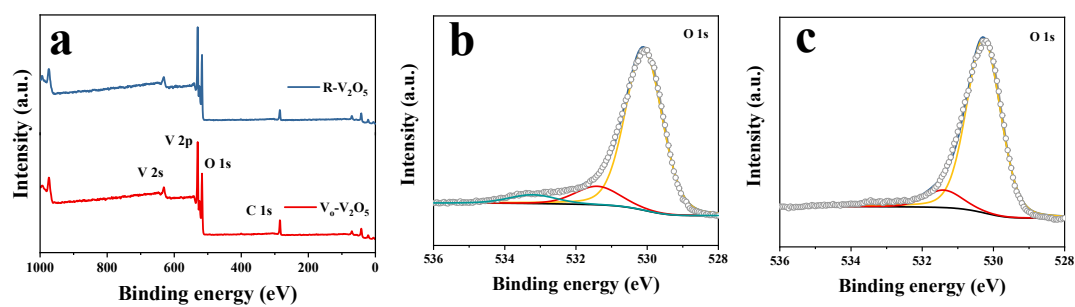


Figure S3. (a) XPS survey scans of the R- V_2O_5 , and V_0 - V_2O_5 . O 1s high-resolution XPS spectra of (b) V_0 - V_2O_5 , and (c) R- V_2O_5 .

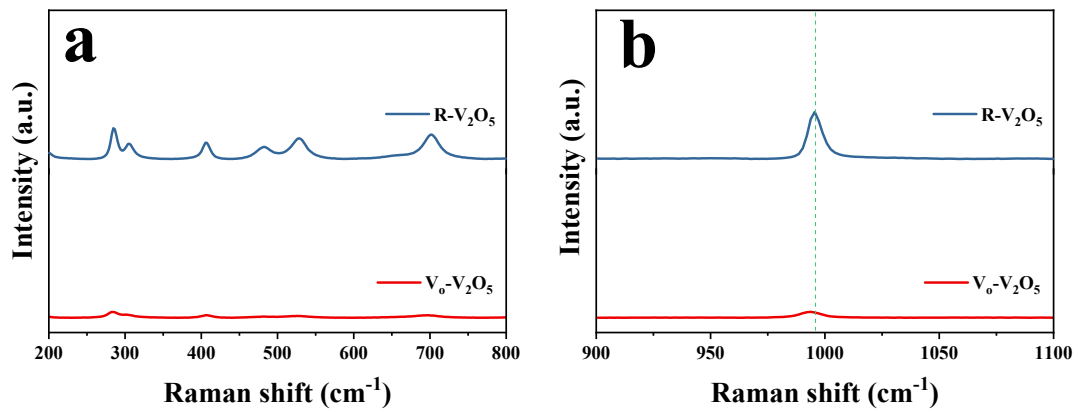


Figure S4. The Raman spectra of the R- V_2O_5 and V_0 - V_2O_5 .

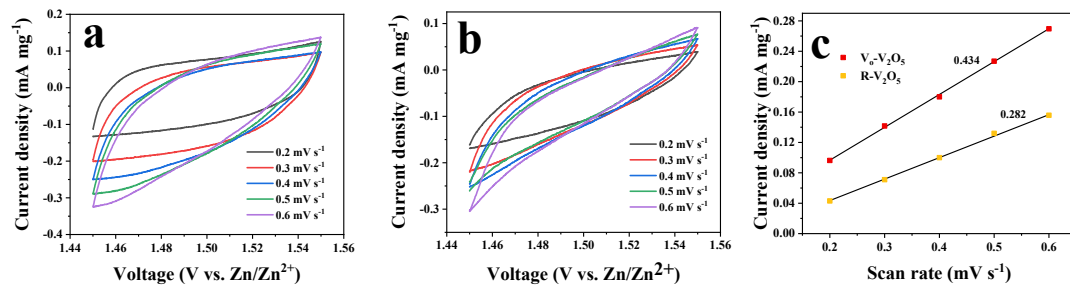


Figure S5. CV curves of current densities versus scan rates of (a) V_0 - V_2O_5 , and (b) R- V_2O_5 . (c) The corresponding linear fit of current densities versus scan rates.

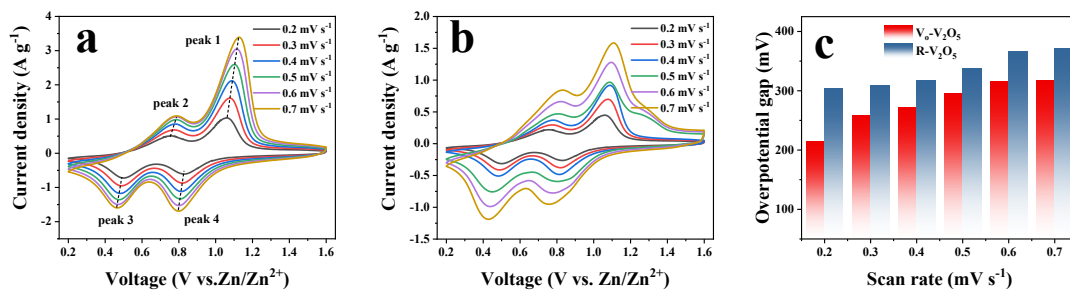


Figure S6. CV curves of current densities versus scan rates of (a) V_0 - V_2O_5 , and (b) R- V_2O_5 . (c) Overpotential gaps of the redox pair for peak 1 and peak 4.

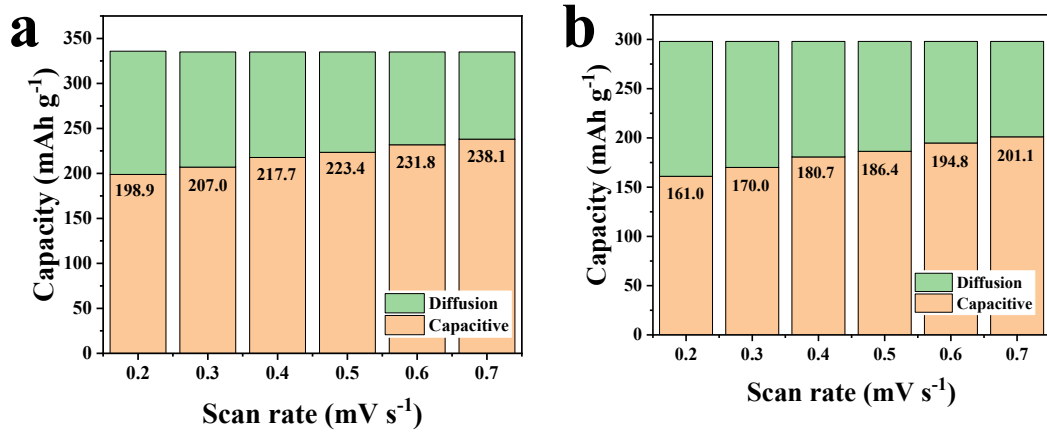


Figure S7. The capacitive contributions at different scan rates of (a) Zn/Vo-V₂O₅, and (b) Zn/R-V₂O₅.

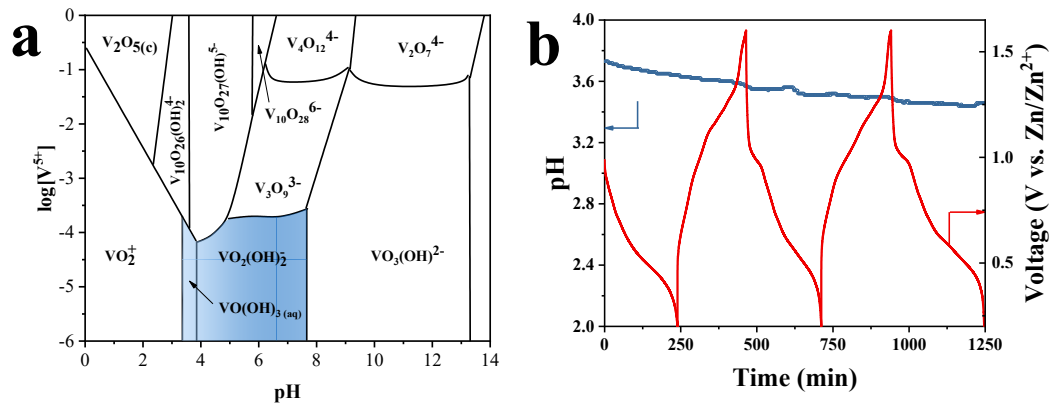


Figure S8. (a) The pH-log [V⁵⁺] diagram in V₂O₅-H₂O system. (b) pH and voltage values vs. the charging/discharging time of V_o-V₂O₅.

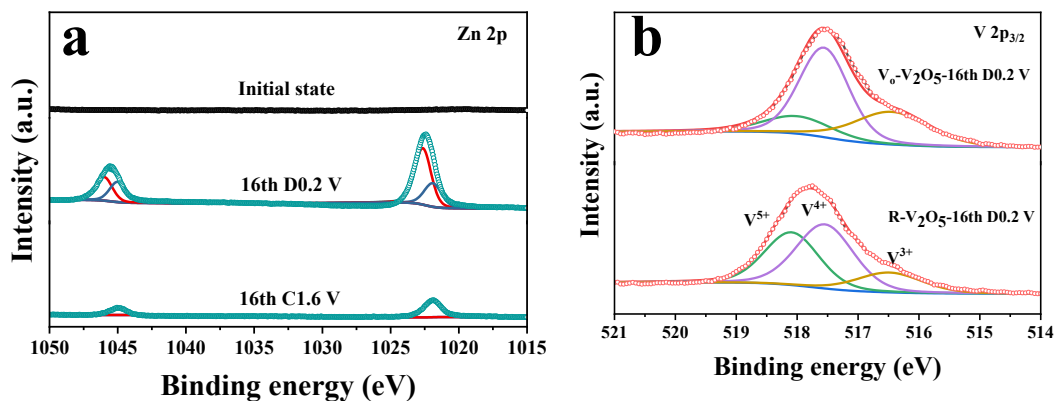


Figure S9. (a) XPS spectra of Zn 2p in initial, fully discharged, and charged states in the 16th cycle. (b) XPS spectra of fully discharged R-V₂O₅, and fully discharged V₀-V₂O₅.

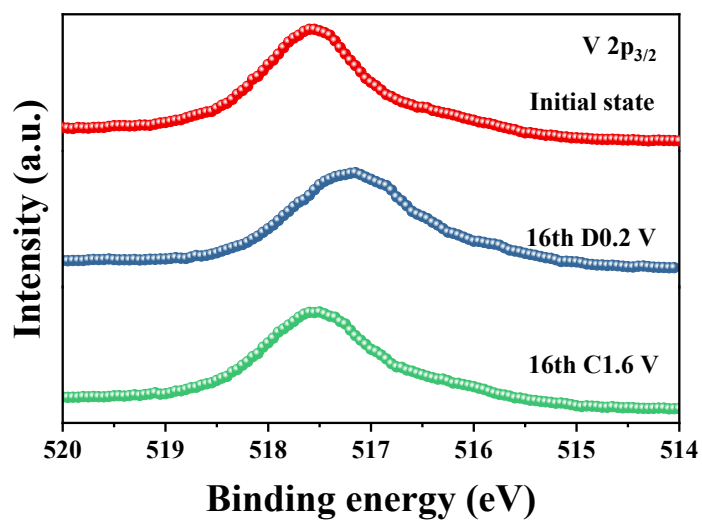


Figure S10. V 2p XPS spectra of the V₀-V₂O₅ at initial state, 16th -D-0.2, and 16th -C-1.6 states, respectively.

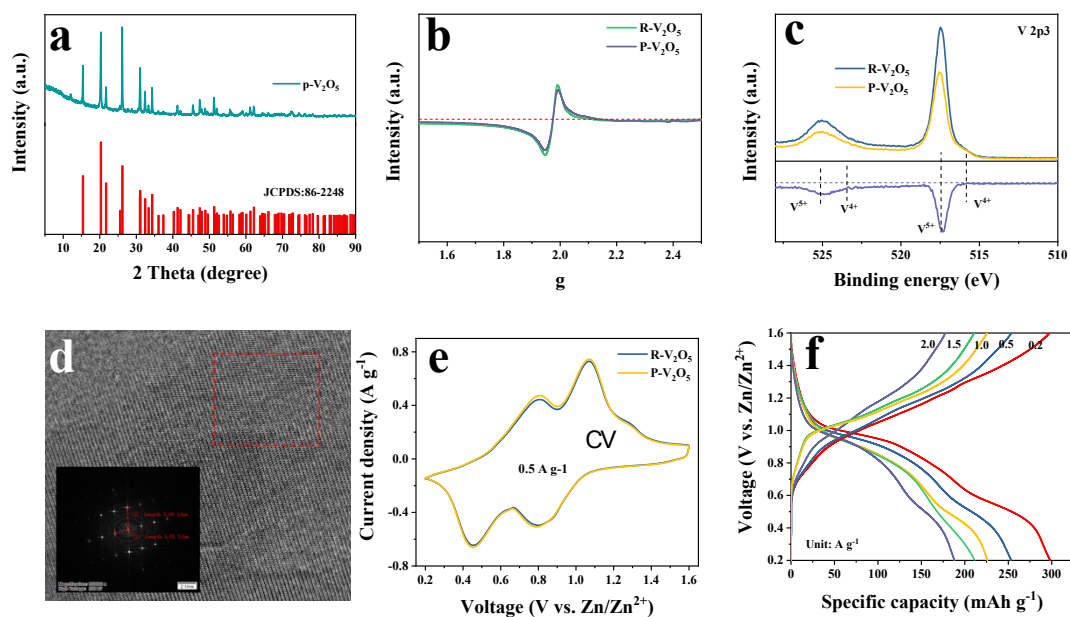


Figure S11. (a) The XRD patterns, (b) ESR spectra, and (c) XPS spectra of P-V₂O₅ and R-V₂O₅. (d) HRTEM image of P-V₂O₅. (e) Comparison of the CV curves of P-V₂O₅ and R-V₂O₅. (f) Galvanostatic discharge profiles of P-V₂O₅ at increasing current densities from 0.2 to 2.0 A g⁻¹.

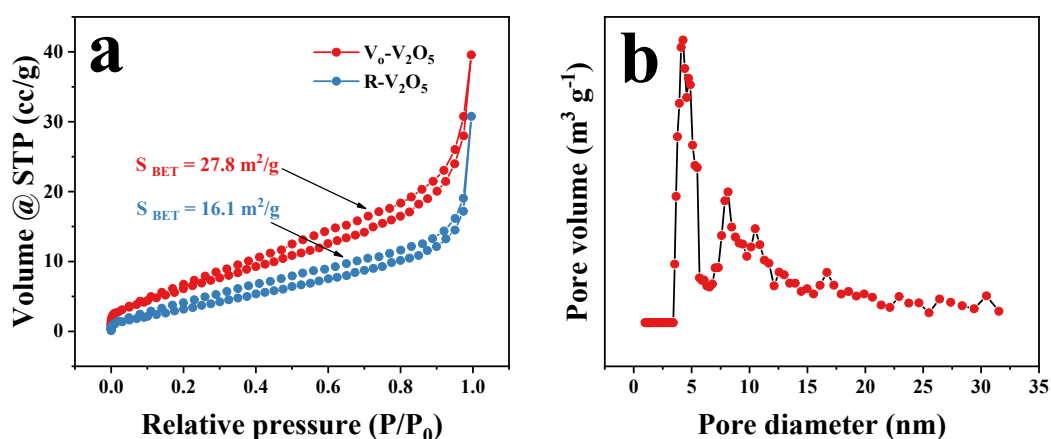


Figure S12. (a) Nitrogen-adsorption isotherms recorded at 77 K for V₀-V₂O₅ and R-V₂O₅. (b) Pore size distribution of V₀-V₂O₅ determined from the adsorption isotherms by using the BJH methods.

The surface area and porosity property were investigated by N₂-adsorption/desorption measurements. The Brunauer-Emmett-Teller (BET) surface area of V_o-V₂O₅ is calculated to be 27.8 mg² g⁻¹, which is substantially higher than that of R-V₂O₅. Besides, the pore size distribution of V_o-V₂O₅, determined using the Barrett-Joyner-Halenda (BJH) method, is centered around 10 nm, confirming that V_o-V₂O₅ possesses a mesoporous character. Such a mesoporous structure provides sufficient surface area to promote electrochemical reactions and efficient penetration of the electrolyte into the active material.

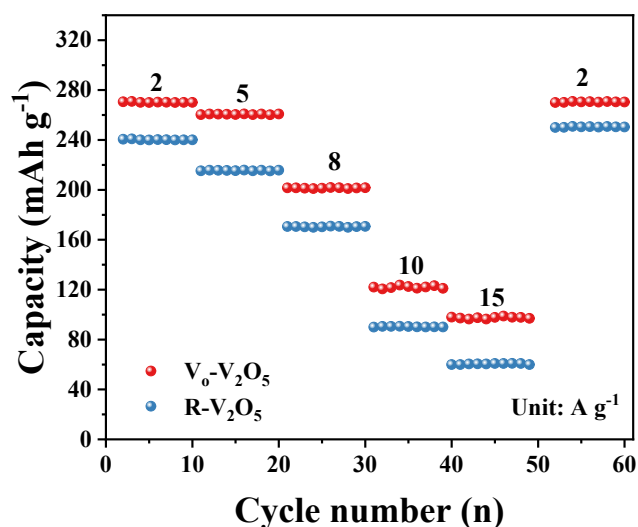


Figure S13. Rate capacities at current densities between 2.0 and 15 A g⁻¹ of V_o-V₂O₅ and R-V₂O₅.

The Figure S13 shows the rate capability at current densities between 2.0 and 15 A g⁻¹ of the V_o-V₂O₅ and R-V₂O₅ electrodes. The reversible capacities of 270, 262, 201, 120 and 97 mA h g⁻¹ were obtained for the V_o-

V_2O_5 electrode at 2, 5, 8, 10 and 15 $A\ g^{-1}$, respectively, and the reversible capacity can be recovered to 268 $mA\ h\ g^{-1}$ when the current density returns to 2 $A\ g^{-1}$, which is obviously higher than that of the R- V_2O_5 .

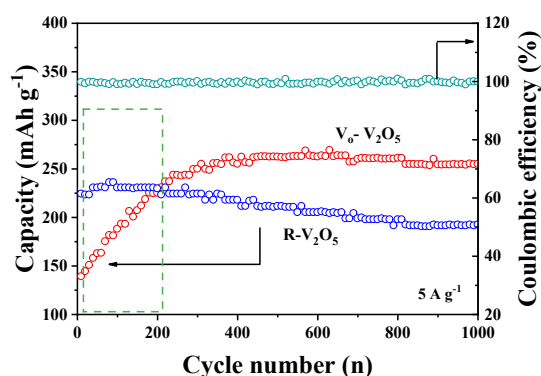


Figure S14. The locally amplified cyclic stability curve of V_o - V_2O_5 and R- V_2O_5 under 5 $A\ g^{-1}$.

As shown in the dashed block diagram in the Figure S14, both V_o - V_2O_5 and R- V_2O_5 undergo an activation process. Unfortunately, for R- V_2O_5 , a rapid degradation in capacity occurs with an increase in the cycle number. To further clarify the reason for the large difference in cycling stability between V_o - V_2O_5 and R- V_2O_5 , the images derived from these experiments are shown in Figure S15.

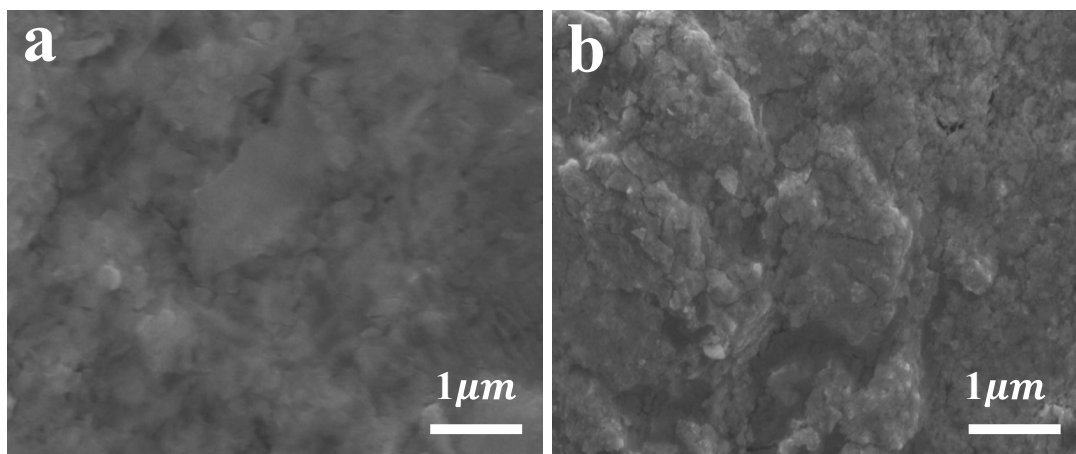


Figure S15. Morphology change of V₂O₅ and R-V₂O₅ positive electrodes after cycling. SEM images of (a) V_o-V₂O₅ and (b) R-V₂O₅ electrodes (5 A g⁻¹, 100th cycle) for Zn/V₂O₅ batteries. Scale bars, 1 μm.

Figure S15 compares the SEM images of V_o-V₂O₅ and R-V₂O₅ electrodes (5 A g⁻¹, 100th cycle) for Zn/V₂O₅ batteries. It is noted that, compared to V_o-V₂O₅ electrodes, after 100 cycles, the R-V₂O₅ electrode shows obvious surface cracks. The large structure changes during the charge/discharge process can lead to structural breakdown and severance of the electrical connection between current collectors. Overall, this results in a rapid and dramatic loss of cell capacity upon cycling. This result indicates that abundant oxygen vacancies introduction well maintains the structural integrity of V₂O₅ during long-term cycling.

Table S1. The content of impurity elements in recycled V_2O_5 (R- V_2O_5)

Element content (wt %)	Cr	Al	Na	K	Ca	Fe	Si
Sample-1	0.003	<0.001	0.003	0.002	0.004	0.003	0.005
Sample-2	0.003	<0.001	0.004	0.003	0.004	0.003	0.006
Sample-3	0.002	<0.001	0.004	0.005	0.008	0.008	0.006

Table S2. Summary of the electrochemical performance of typical vanadium oxides with the different crystal structures and different electrolytes in rechargeable aqueous ZIBs.

Cathode material	Electrolyte		Capacity (mAh g ⁻¹)	Cycle number	Energy density (Wh kg ⁻¹)	Ref.
$V_0-V_2O_5$	3 Zn(CF ₃ SO ₃) ₂	M	375 (0.1 A g ⁻¹)	3500 (5.0 A g ⁻¹ ; 87.2%)	280.6	This Work
$Mn_{1.4}V_{10}O_{24} \cdot 12H_2O$	3 Zn(CF ₃ SO ₃) ₂	M	456 (0.2 A g ⁻¹)	5000 (10 A g ⁻¹ ; 80%)	214	[4]
$Ca_{0.25}V_2O_5 \cdot nH_2O$	3 Zn(CF ₃ SO ₃) ₂	M	340 (0.2 C)	3000 (80 C; 96%)	267	[5]
$K_{0.23}V_2O_5$	2 Zn(CF ₃ SO ₃) ₂	M	284 (0.1 A g ⁻¹)	500 (2.0 A g ⁻¹ ; 92.8%)	-	[6]
PANI100-V_2O_5	3 Zn(CF ₃ SO ₃) ₂	M	360 (0.5 A g ⁻¹)	2000 (5 A g ⁻¹ ; 75.6%)	-	[7]
VN_xO_y	3 M ZnSO ₄		310 (0.1 A g ⁻¹)	300 (1 A g ⁻¹ ; 88.6%)	-	[8]
Ag-doped V_2O_5	3 Zn(CF ₃ SO ₃) ₂	M	200 (0.1 A g ⁻¹)	700 (3 A g ⁻¹ ; 90%)	118	[9]
$Zn_2V_2O_7$	1 M ZnSO ₄		231 (0.1 A g ⁻¹)	1000 (4 A g ⁻¹ ; 85%)	166	[10]
$V_2O_5 \cdot nH_2O/V_3O_7 \cdot nH_2O$	2 M ZnSO ₄		455 (0.1 A g ⁻¹)	1200 (0.5 A g ⁻¹ ; 85%)	340	[11]
Vanadium	3 M ZnSO ₄		256	1000	-	[12]

oxide fibers			(1.0 A g ⁻¹)	(5.0 A g ⁻¹ ; 83%)		
Ni_{0.25}V₂O₅·0.88	3	M	418	10000	300	[13]
H₂O	Zn(CF ₃ SO ₃) ₂		(0.155 A g ⁻¹)	(10 A g ⁻¹ ; 77%)		
VO₂	3	M	274	10000	271.8	[14]
	Zn(CF ₃ SO ₃) ₂		(0.1 A g ⁻¹)	(20 C; 79%)		
V₂O_x@V₂CT_x	1 M ZnSO ₄		304	200	228	[15]
			(0.05 A g ⁻¹)	(1.0 A g ⁻¹ ; 81.6%)		
Vanadium oxide nanotubes						
H₁₁Al₂V₆O_{23.2}	3	M	288.4	7000	243	[17]
	Zn(CF ₃ SO ₃) ₂		(0.1 A g ⁻¹)	(5.0 A g ⁻¹ ; 88.6%)		
S-NVOH	3 M (Zn(TfO) ₂)		108	1000	-	[18]
			(2 A g ⁻¹)	(2 A g ⁻¹ ; 91%)		
Layered VOH (VO₂·0.5H₂O)	2	M	268	240	-	[19]
	Zn(CF ₃ SO ₃) ₂		(50 mA g ⁻¹)	(50 mA g ⁻¹ ; 88%)		
C@V₂O₅	3	M	361	2000	-	[20]
	Zn(CF ₃ SO ₃) ₂		(0.5 A g ⁻¹)	(0.5 A g ⁻¹ ; 71%)		

References

- [1] P. Ning, X. Lin, X. Wang, H. Cao, High-efficient extraction of vanadium and its application in the utilization of the chromium-bearing vanadium slag, *Chem. Eng. J.* 301 (2016) 132-138. <https://doi.org/10.1016/j.cej.2016.03.066>.
- [2] X. Jing, P. Ning, H. Cao, Z. Sun, J. Wang, Separation of V(V) and Cr(VI) in leaching solution using annular centrifugal contactors, *Chem. Eng. J.* 315 (2017) 373-381. <https://doi.org/10.1016/j.cej.2017.01.014>.
- [3] J. Wen, P. Ning, H. Cao, Z. Sun, Y. Zhang, G. Xu, Recovery of high-purity vanadium from aqueous solutions by reusable primary amines N1923 associated with semiquantitative understanding of vanadium species, *ACS Sustainable Chem. Eng.* 6(6) (2018) 7619-7626. <https://doi.org/10.1021/acssuschemeng.8b00445>.
- [4] H. Chen, J. Huang, S. Tian, L. Liu, T. Qin, L. Song, Y. Liu, Y. Zhang, X. Wu, S. Lei, S. Peng, Interlayer modification of pseudocapacitive vanadium oxide and Zn(H₂O)_n²⁺ migration regulation for ultrahigh rate and durable aqueous zinc-ion batteries, *Adv. Sci.* 8(14) (2021) e2004924. <https://doi.org/10.1002/advs.202004924>.
- [5] C. Xia, J. Guo, P. Li, X. Zhang, H.N. Alshareef, Highly stable aqueous zinc-ion storage using a layered calcium vanadium oxide bronze cathode, *Angew. Chem., Int. Ed.* 57(15) (2018) 3943-3948. <https://doi.org/10.1002/anie.201713291>.
- [6] W. Zhang, C. Tang, B. Lan, L. Chen, W. Tang, C. Zuo, S. Dong, Q. An, P. Luo, K_{0.23}V₂O₅ as a promising cathode material for rechargeable aqueous zinc ion batteries with excellent performance, *J. Alloys Compd.* 819 (2020) 152971. <https://doi.org/10.1016/j.jallcom.2019.152971>.
- [7] S. Chen, K. Li, K.S. Hui, J. Zhang, Regulation of lamellar structure of vanadium oxide via polyaniline

- intercalation for high-performance aqueous zinc-ion battery, *Adv. Funct. Mater.* 30(43) (2020) 2003890. <https://doi.org/10.1002/adfm.202003890>.
- [8] X. Xie, G. Fang, W. Xu, J. Li, M. Long, S. Liang, G. Cao, A. Pan, In situ defect induction in close-packed lattice plane for the efficient zinc ion storage, *Small* (2021) e2101944. <https://doi.org/10.1002/sml.202101944>.
- [9] B. Lan, Z. Peng, L. Chen, C. Tang, S. Dong, C. Chen, M. Zhou, C. Chen, Q. An, P. Luo, Metallic silver doped vanadium pentoxide cathode for aqueous rechargeable zinc ion batteries, *J. Alloys Compd.* 787 (2019) 9-16. <https://doi.org/10.1016/j.jallcom.2019.02.078>.
- [10] B. Sambandam, V. Soundharajan, S. Kim, M.H. Alfaruqi, J. Jo, S. Kim, V. Mathew, Y.-k. Sun, J. Kim, Aqueous rechargeable Zn-ion batteries: an imperishable and high-energy $Zn_2V_2O_7$ nanowire cathode through intercalation regulation, *J. Mater. Chem. A* 6(9) (2018) 3850-3856. <https://doi.org/10.1039/c7ta11237h>.
- [11] X. Li, L. Ma, Y. Zhao, Q. Yang, D. Wang, Z. Huang, G. Liang, F. Mo, Z. Liu, C. Zhi, Hydrated hybrid vanadium oxide nanowires as the superior cathode for aqueous Zn battery, *Mater. Today Energy* 14 (2019) 100361. <https://doi.org/10.1016/j.mtener.2019.100361>.
- [12] Z. Chen, J. Hu, S. Liu, H. Hou, G. Zou, W. Deng, X. Ji, Dual defects boosting zinc ion storage of hierarchical vanadium oxide fibers, *Chem. Eng. J.* 404 (2021) 126536. <https://doi.org/10.1016/j.cej.2020.126536>.
- [13] J. Feng, Y. Wang, S. Liu, S. Chen, N. Wen, X. Zeng, Y. Dong, C. Huang, Q. Kuang, Y. Zhao, Electrochemically induced structural and morphological evolutions in nickel vanadium oxide hydrate nanobelts enabling fast transport kinetics for high-performance zinc storage, *ACS Appl. Mater. Interfaces* 12(22) (2020) 24726-24736. <https://doi.org/10.1021/acsami.0c04199>.
- [14] T. Wei, Q. Li, G. Yang, C. Wang, An electrochemically induced bilayered structure facilitates long-life zinc storage of vanadium dioxide, *J. Mater. Chem. A* 6(17) (2018) 8006-8012. <https://doi.org/10.1039/c8ta02090f>.
- [15] R. Venkatkarthick, N. Rodthongkum, X. Zhang, S. Wang, P. Pattanauwat, Y. Zhao, R. Liu, J. Qin, Vanadium-based oxide on two-dimensional vanadium carbide MXene ($V_2O_x@V_2CT_x$) as cathode for rechargeable aqueous zinc-ion batteries, *ACS Appl. Energy Mater.* 3(5) (2020) 4677-4689. <https://doi.org/10.1021/acsaem.0c00309>.
- [16] F. Yang, Y. Zhu, Y. Xia, S. Xiang, S. Han, C. Cai, Q. Wang, Y. Wang, M. Gu, Fast Zn^{2+} kinetics of vanadium oxide nanotubes in high-performance rechargeable zinc-ion batteries, *J. Power Sources* 451 (2020) 227767. <https://doi.org/10.1016/j.jpowsour.2020.227767>.
- [17] T. Wei, Y. Liu, G. Yang, C. Wang, Aluminum vanadate hollow spheres as zero-strain cathode material for highly reversible and durable aqueous zinc-ion batteries, *Energy Storage Materials* 30 (2020) 130-137. <https://doi.org/10.1016/j.ensm.2020.04.039>.
- [18] J. Zhang, M. Wang, M. Zeng, X. Li, L. Chen, Z. Yang, J. Chen, B. Guo, Z. Ma, X. Li, Sulfite modified and ammonium ion intercalated vanadium hydrate with enhanced redox kinetics for aqueous zinc ion batteries, *J. Power Sources* 496 (2021) 229832. <https://doi.org/10.1016/j.jpowsour.2021.229832>.
- [19] B. Ju, H.J. Song, H. Yoon, D.-W. Kim, Amorphous hydrated vanadium oxide with enlarged interlayer spacing for aqueous zinc-ion batteries, *Chem. Eng. J.* 420 (2021) 130528. <https://doi.org/10.1016/j.cej.2021.130528>.
- [20] C. Liu, R. Li, W. Liu, G. Shen, D. Chen, Chitosan-assisted fabrication of a network $C@V_2O_5$ cathode for high-performance Zn-ion batteries, *ACS Appl. Mater. Interfaces* 13(31) (2021) 37194-37200. <https://doi.org/10.1021/acsaem.1c09951>.

